

## RESEARCH ARTICLE

10.1002/2014JD021717

## Key Points:

- A new CloudSat cloud object is introduced
- Several anvil sensitivities to sea surface temperature are examined
- A new anvil sensitivity to sea surface temperature is introduced

## Correspondence to:

M. R. Igel,  
mattigel@atmos.colostate.edu

## Citation:

Igel, M. R., A. J. Drager, and S. C. van den Heever (2014), A CloudSat cloud object partitioning technique and assessment and integration of deep convective anvil sensitivities to sea surface temperature, *J. Geophys. Res. Atmos.*, 119, 10,515–10,535, doi:10.1002/2014JD021717.

Received 6 MAR 2014

Accepted 24 AUG 2014

Accepted article online 27 AUG 2014

Published online 15 SEP 2014

## A CloudSat cloud object partitioning technique and assessment and integration of deep convective anvil sensitivities to sea surface temperature

Matthew R. Igel<sup>1</sup>, Aryeh J. Drager<sup>1</sup>, and Susan C. van den Heever<sup>1</sup>

<sup>1</sup>Department of Atmospheric Science, Colorado State University, Fort Collins, Colorado, USA

**Abstract** A cloud object partitioning algorithm is developed to provide a widely useful database of deep convective clouds. It takes contiguous CloudSat cloudy regions and identifies various length scales of clouds from a tropical, oceanic subset of data. The methodology identifies a level above which anvil characteristics become important by analyzing the cloud object shape. Below this level in what is termed the pedestal region, convective cores are identified based on reflectivity maxima. Identifying these regions allows for the assessment of length scales of the anvil and pedestal of deep convective clouds. Cloud objects are also appended with certain environmental quantities from European Centre for Medium-Range Weather Forecasts. Simple geospatial and temporal assessments show that the cloud object technique agrees with standard observations of local frequency of deep convective cloudiness. Deep convective clouds over tropical oceans play important roles in Earth's climate system. The newly developed data set is used to evaluate the response of tropical, deep convective clouds to sea surface temperature (SST). Several previously proposed responses are examined: the Fixed Anvil Temperature Hypothesis, the Iris Hypothesis, and the Thermostat Hypothesis. When the data are analyzed per cloud object, increasing SST is found to be associated with increased anvil thickness, decreased anvil width, and cooler cloud top temperatures. Implications for the corresponding hypotheses are discussed. A new response suggesting that the base temperature of deep convective anvils remains approximately constant with increasing SSTs is introduced. These cloud dependencies on SST are integrated to form a more comprehensive theory for deep convective anvil responses to SST.

### 1. Introduction

Convective clouds are perhaps the most easily observed aspect of the tropical atmospheric system by the layman. But thorough, scientific observation of convective clouds is difficult. Clouds are frequent over ocean, away from ground-based observation systems; they occur across a wide range of length scales, creating difficulty for models; and scientifically defining precisely what is and what is not a cloud remains an elusive goal. Little literature exists on the range of scales over which tropical convection tends to occur, yet if predictions of climate change and weather are to be made more accurate, some knowledge of these scales, the manner in which they interact, and the ways in which they might change with warming is imperative [Stephens, 2005]. Some of the most crucial climate and weather impacts of clouds cannot be understood without knowledge of their physical length scales [Bony *et al.*, 2006]. The height, and therefore cloud top temperature, of deep convective clouds dictates the net amount of radiation emitted from the climate system at the top of the atmosphere to space and consequently the amount absorbed by the atmosphere [Manabe and Strickler, 1964]. Likewise, the depth of convective anvils defines their shortwave reflectivity [Liou, 1996], and the width of convective anvils determines the partitioning between radiation emitted from high, cold clouds to that from shallow clouds or low, warm regions of clear sky [Stephens *et al.*, 2008].

Extensive previous theoretical and observational work has investigated the interactions between climate and deep convective morphology. Focusing on different facets of these interactions, previous studies have hypothesized and measured how clouds respond to climatologically warmer sea surface temperatures (SSTs):

1. The Thermostat Hypothesis was originally proposed by Ramanathan and Collins [1991]. As the name suggests, it is a theory that attempts to explain the self-regulation of surface temperature in the tropics.

*Ramanathan and Collins* [1991] compared data collected during a warm phase of El Niño to data taken during an unperturbed period. They found that the reflectivity of cirrus anvils was greater during the warmer SST (El Niño) period. This led them to propose a negative climate feedback between cirrus anvils and SSTs in which a warmer environment creates thicker anvil cirrus and is subsequently cooled by the more reflective cirrus. Recent observational work [*Lebock et al.*, 2010; *Lloyd et al.*, 2012] has supported this hypothesis.

2. The Iris Hypothesis of *Lindzen et al.* [2001] suggests that as SST increases, the mean anvil area of convective systems will decrease per convective system. This is proposed to occur through an increase in precipitation efficiency (the ratio of water mass precipitated out of cloud base to water vapor fluxed into the base of the cloud). The proposed result is a net negative climate feedback composed of two competing processes: cooling through increased longwave emission (dominant) and warming through lessened shortwave reflectance. This hypothesis has been widely contested [e.g., *Del Genio and Kovari*, 2002; *Lin et al.*, 2004], often based on the validity of observational evidence rather than the plausibility of the proposed physical mechanisms.
3. The Fixed Anvil Temperature (FAT) Hypothesis of *Hartmann and Larson* [2002] proposes a constant emission temperature from deep convection regardless of the climate state and SST. FAT has shown to be reproducible in models [*Kuang and Hartmann*, 2007], if not without limitations [*Harrop and Hartmann*, 2012]. However, it has been suggested that cloud top temperature might actually increase with increasing surface temperature in the Proportionally Higher Anvil Temperature (PHAT) conjecture [*Zelinka and Hartmann*, 2010] due to changes in mean static stability. FAT has been assessed observationally [*Li et al.*, 2012]. *Xu et al.* [2007] showed FAT to be approximately true for horizontally large clouds. And, similar, though conceptually different attempts than those described here have been made to relate CloudSat object-clusters to SST [*Behrangi et al.*, 2012].

Although all of these hypotheses link cloud top and anvil properties to SST, they generally do not propose how changes in SST might affect cloud morphology below cloud top. This is not entirely surprising given the relative ease of observing cloud top properties from space and the difficulties in obtaining any information below cirrus shields, and since at first glance, below-top quantities would seem to be less important to understanding climate forcing than to detailing convective processes. Indeed, this is not entirely untrue. However, convective processes are important to climate and weather when they feed up scale, either through the general circulation mass balance or through the effects on the moisture field and precipitation [*Randall et al.*, 2003; *Stevens*, 2005; *Igel et al.*, 2014].

This work will describe the development of a new CloudSat-derived database and seek evidence for the existence or absence of 1–3 within this data set. A potential new SST-cloud relationship will also be suggested. These responses of anvils to SST will be discussed as a single-cloud morphological response.

## 2. Data and Methods

The idea of dissecting scenes of remotely sensed cloud data into contiguous “pieces” of cloud is not new. Such “cloud object” techniques have been used successfully in a variety of different ways. Infrared or visible data from geostationary or polar orbiting satellites have been separated into cloudy and clear sky regions [e.g., *Xu et al.*, 2005; *Dias et al.*, 2012]. The horizontal lengths or areas of clouds within the scene have then been analyzed. The idea can be taken a step further by joining several data sources that cover the same area in order to utilize instrument benefits [e.g., *Nesbitt et al.*, 2000]. Cloud objects have also been defined in the vertical through the use of active sensors [e.g., *Nesbitt et al.*, 2000; *Riley et al.*, 2011; *Bacmeister and Stephens*, 2011]. In this case, the cloud object represents a vertical slice or cross section through the cloud. Because these objects provide details in the vertical plane, information about the vertical distribution of liquid water or ice or the effective width of a convective core may be obtained, for example. Fundamentally, the cloud object method can be used to define separate, contiguous cloudy regions and then to understand the physical properties of different groups of objects.

This work introduces a new CloudSat cloud object data set designed for use in investigations of deep convective clouds. While it was inspired by the work of *Bacmeister and Stephens* [2011] who sought to partition clouds into some of the same components that this research does, the methods utilized are very different. The basic goal in constructing this data set is for it to be purposefully inclusive of deep convective

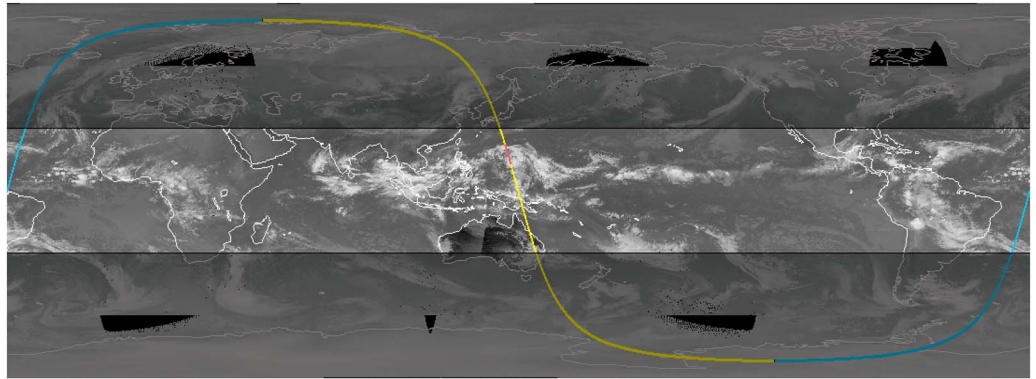


**Figure 1.** The orbital path for CloudSat granule 7919, obtained on 24 October 2007, superimposed on global infrared satellite imagery. The orbital path proceeds from right to left, with a nighttime (blue path) equator crossing over the Atlantic Ocean, a daytime (yellow path) equator crossing in the western Pacific Ocean, and a nighttime equator crossing over South America. The tropics, defined as 30°S–30°N, are highlighted. The data for the next several figures are taken from the red section of the path.

clouds so as not to allow preconceptions about their size and shape to influence any results. Some of the selection criteria could be further refined in order to limit objects to a certain life cycle stage, say, but this is not the present objective. Following a brief description of the raw data, a discussion of data processing will be conducted. This will include the details, justification, and assessment of the filtering methods used to determine which raw data are included in the final data set. A detailed description of the new deep convective pedestal/ anvil separation algorithm with examples will follow.

## 2.1. Data

The methodology developed herein uses a combination of observational data based on retrievals from the CloudSat 94 GHz cloud profiling radar (CPR) and colocated European Centre for Medium-Range Weather Forecasts (ECMWF) environmental reanalysis data. CloudSat is part of the A-Train constellation of satellites and utilizes a Sun-synchronous orbit that crosses the equator at approximately 0130 and 1330 local time [Stephens *et al.*, 2002]. The CloudSat radar is designed to observe cloud vertical structure and samples clouds with a vertical resolution of approximately 500 m, a cross-track resolution of approximately 1.4 km, and an along-track resolution of approximately 1.8 km [Stephens *et al.*, 2008]. Data are oversampled such that radar reflectivity and other profiles are reported with vertical spacing of 240 m and along-track spacing of 1079 m. The CloudSat Data Processing Center provides CloudSat data in granules, where one granule contains retrievals taken between two successive nighttime (0130 local time) equator crossings. Figure 1 shows one such granule, obtained on 24 October 2007. Complete information regarding CloudSat capabilities and data products may be obtained from the CloudSat Data Processing Center (<http://cloudsat.cira.colostate.edu>).

Data available at the time of this study span from the start of CloudSat CPR operation in June 2006 to a temporary system shutdown in April 2011. The present analysis makes use of the level-2 2B-GEOPROF [Haynes and Stephens, 2007], 2B-CLDCLASS [Wang and Sassen, 2007], 2B-CWC-RVOD [Wood, 2008], 2B-FLXHR [L'Ecuyer *et al.*, 2008], and 2B-TAU [Polonsky *et al.*, 2008] CloudSat products, along with the ECMWF-AUX and ECMWF2-AUX [Partain, 2007] auxiliary data products. After elimination of the small minority of granules for which at least one of these data products is unavailable, the data set comprises approximately 20,000 granules. In keeping with the intended uses of this data set, analyses are limited to retrievals taken over tropical latitudes, defined here as 30°S–30°N (unshaded section of Figure 1). Since a single granule comprises retrievals taken between successive nighttime equator crossings (see Figure 1), each granule contains three tropical sections: one tropical section at each end of the granule, associated with the successive nighttime equator crossings (blue line in Figure 1), and one central tropical section, associated with the daytime equator crossing (yellow in Figure 1). For this study, we have chosen to limit our analysis to the central tropical section of each granule. This choice effectively eliminates half of all available Cloudsat data but provides several benefits. We have observed that the edges of some granules are missing one or more columns of data which could lead to underestimation of cloud size; one benefit of considering only the central tropical section of each granule is that the potential error associated with attempting to stitch edges

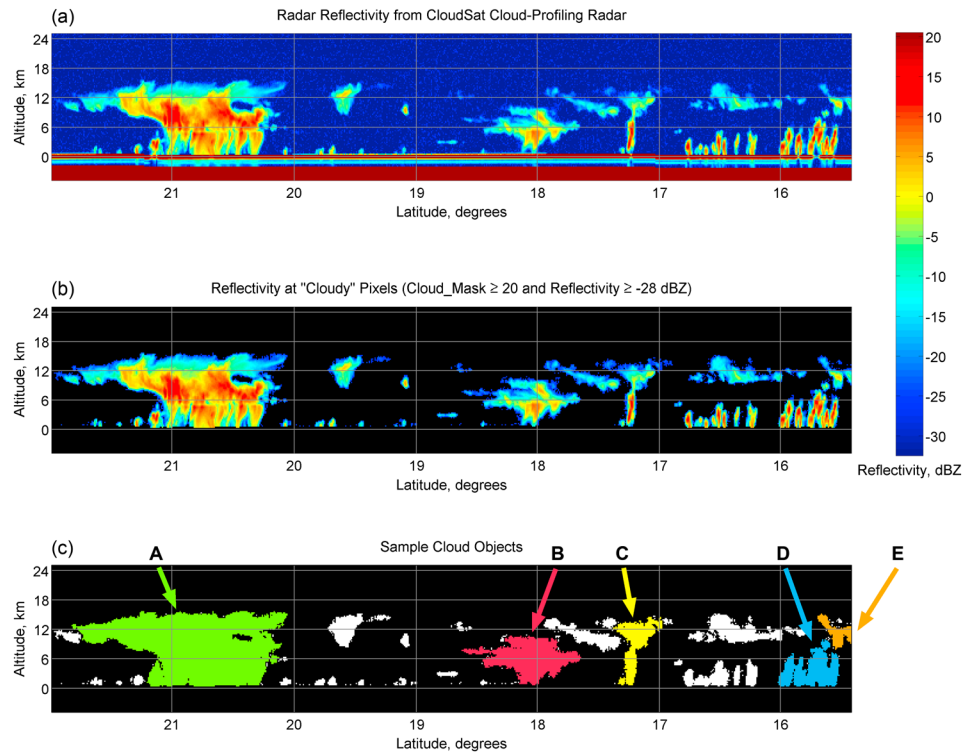


**Figure 2.** Partial daytime tropical retrieval from CloudSat granule 7919 (shown in Figure 1). (a) The 2B-GEOPROF Radar\_Reflectivity field. (b) Same as Figure 2a but with clear pixels colored black. (c) Cloud objects within the retrieval. Cloud objects meeting basic vertical extent requirements are colored and labeled for reference within our discussion. A more complete view of object E (orange) is provided in Figure 3.

of adjacent granules together is avoided. Throughout the development of this methodology, data will be pared away, sometimes seemingly excessively so (like the decision to eliminate nighttime data). However, the data set is still highly inclusive as the sheer amount of data available from 5 years of CloudSat allows for powerful statistics even with a limited subset of data.

A consequence of the A-Train's orbit is that all retrievals over tropical latitudes are taken along a track that has a large meridional component and a small zonal component. Thus, implicit in this and other analyses of tropical CloudSat retrievals [e.g., Bacmeister and Stephens, 2011] is the assumption that tropical clouds possess no systematic anisotropy in the horizontal. We have no reason to reject this assumption in the ensemble mean, although individual clouds can be highly anisotropic. Additional effects of meridional sampling are discussed when relevant.

## 2.2. Methods

An object-based approach similar to that of Bacmeister and Stephens [2011] is employed to identify cloud objects within each CloudSat granule. A more general discussion of object-oriented analysis approaches is provided in Sellars et al. [2013]. After cloud objects are identified, a number of filters are applied in order to select mature, marine, deep convective cloud objects for further analysis. Steps are then taken to help to analyze the morphology of each of these cloud objects. First, each cloud object is partitioned into a convective "pedestal" region and an upper "anvil" region (see section 2.2.2 for definitions). A core-counting algorithm is applied in order to estimate the number of convective cores within each cloud object's pedestal region. Following this preparation, steps are taken to evaluate heights and widths corresponding to various morphological attributes and reanalysis data are used to quantify different environmental attributes (e.g., sea surface temperature) associated with each cloud object.

Throughout much of the discussion to follow, a sample cloud scene will be examined to illustrate the development of the methodology. The satellite plan view in Figure 1 provides high-level context for this scene. Figure 2a shows the raw reflectivity observed by CloudSat over a select portion of the daytime tropical

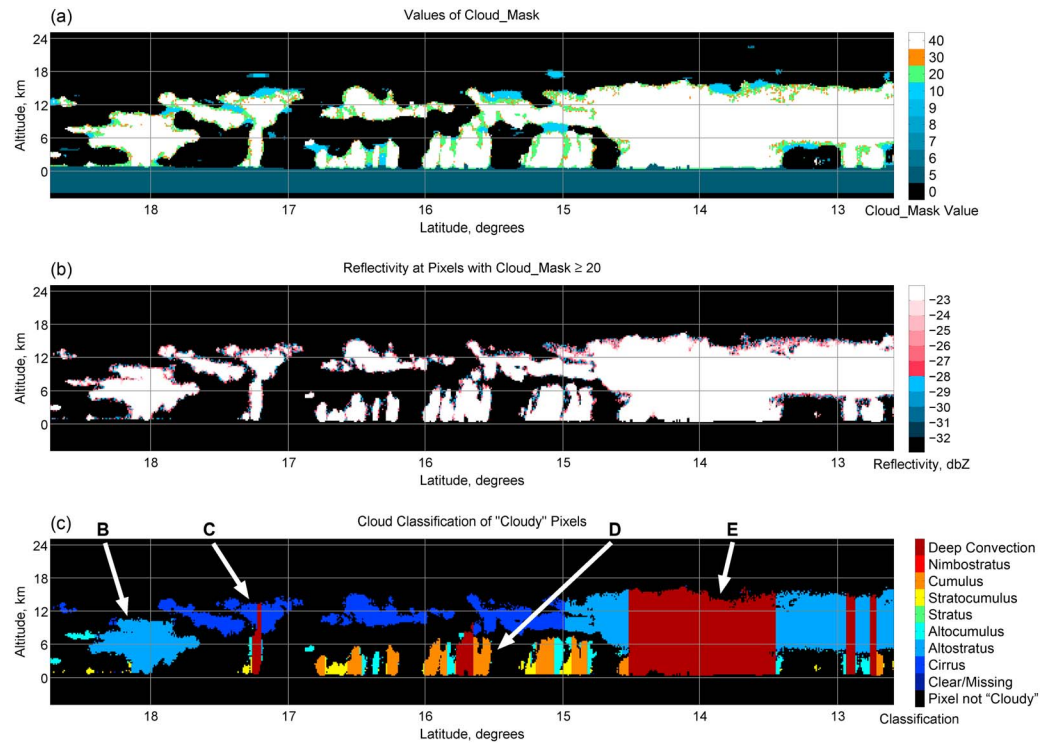


**Figure 3.** Illustration of various filtering mechanisms and thresholds. Note the overlap between this scene and that shown in Figure 2. (a) The 2B-GEOPROF “CPR\_Cloud\_mask” field. By our choice of threshold, pixels with values of 20, 30, and 40 are retained. (b) Same as Figure 2b, with color scale modified to emphasize pixels with low reflectivity. By our choice of threshold, pixels with reflectivities of at least  $-28$  dBZ<sub>e</sub> (shown in red) are retained. (c) Values of the 2B-CLDCLASS cloud\_scenario field for cloudy pixels.

domain shown in Figure 1. Subsequent parts of Figure 2 will be discussed when relevant. The colored cloud objects labeled in Figure 2c will be the primary targets of discussion.

### 2.2.1. Identifying Cloud Objects

The 2B-GEOPROF [Haynes and Stephens, 2007] “Radar\_Reflectivity” and “CPR\_Cloud\_mask” fields are used to designate each pixel within the data set as “cloudy” or “clear.” Equivalently, the binary function  $C(j,k)$  for horizontal index  $j$  and vertical index  $k$  such that  $C(j,k) = 1$  for cloudy pixels and  $C(j,k) = 0$  for clear pixels is created. Individual cloud objects are then defined as regions of contiguous cloudy pixels, where pixels are considered contiguous if they share an edge but not if they share a only corner. A pixel is designated as cloudy if, and only if, its Radar\_Reflectivity value is at least  $-28$  dBZ and its CPR\_Cloud\_mask value is at least 20. This Radar\_Reflectivity threshold is approximately equal to the CloudSat CPR’s minimum detectable signal, and this CPR\_Cloud\_mask threshold corresponds to approximately 95% confidence that the detected signal is not the result of noise [Mace, 2006]. A mask of 20 is a commonly used threshold [e.g., Sassen and Wang, 2008; Riley and Mapes, 2009]. Significantly, more rigid thresholds eliminate anvil pixels too aggressively, producing anvil regions detached from their parent convective cores, while significantly more permissive thresholds result in many clearly independent cloud objects becoming connected by bridges of questionably cloudy pixels, especially in the anvil. Figures 3a and 3b illustrate the effects of various threshold choices on the cloud objects that result. These figures show that the thresholds listed above serve effectively to screen out data that are unlikely to be cloud without paring away too much data. As an anecdotal example, in the scenario illustrated in Figures 2 and 3, more permissive thresholds would have resulted in the seemingly inappropriate incorporation of object D into object E. More rigid thresholds might have resulted in the separation of the highest-altitude cloudy region near 15°N from object E. The overall results were tested for a range of numerical thresholds and were found to be insensitive to the choices made. It may therefore be assumed that the conclusions drawn in section 4 are robust in this regard.

Each CloudSat granule contains potentially hundreds of cloud objects. From these, likely mature, deep convective cloud objects over tropical oceans are selected for further analysis. To be selected, a cloud object must satisfy *all* of the following criteria:

1. The cloud object must be contained entirely within the central tropical section of the granule. If a granule is incomplete and has an edge within the daytime tropical part of the orbit, objects intersecting the edge of the granule are excluded so as to eliminate incomplete cloud objects.
2. The cloud object must lie entirely over water. This criterion is enforced using the "Navigation\_land\_sea\_flag" information provided by the 2B-GEOPROF product.
3. The cloud object must have significant vertical extent, extending down at least to the 100<sup>th</sup> vertical level (out of 125, corresponding to an average height of approximately 1.2 km above ground level (agl)) and extending up to at least the 64<sup>th</sup> vertical level (corresponding to an average height of approximately 9.8 km agl). Although 1.2 km may seem too low a threshold given the possibility of elevated convection, we have observed that nearly all CloudSat deep convective cloud objects over tropical oceans satisfy this condition, as signals from rain result in near-uniform coverage of cloudy pixels at low heights. The five cloud objects identified in Figure 2c satisfy all of the criteria listed thus far (note that object E continues Figure 3c).
4. The cloud object must contain at least one pixel designated as "deep convection" by the 2B-CLDCLASS "cloud\_scenario" field [Wang and Sassen, 2007]. This criterion is primarily a fail-safe, but as Figure 2c shows, object B (red), whose pixels are classified primarily as altostratus, does not satisfy this requirement. Although this criterion only removes about 6% of cloud objects not removed by the other filters, we have observed that it preferentially removes cloud objects that subjectively do not qualify as mature, deep convective cloud objects, such as those resembling object B and those formed by immature convective plumes expanding into preexisting high clouds.
5. The cloud object-partitioning algorithm must identify an anvil region, and the core-counting algorithm must identify at least one convective core. These criteria eliminate objects D (blue) and C (yellow), respectively, and are described further in the next two sections.

Criteria 1 and 2 both introduce a bias toward the over representation of small objects. However, given the comparatively small size of the clouds to the average continuous sampling length, this bias should be small.

### 2.2.2. Partitioning Cloud Objects

Deep convective clouds are those that exhibit several characteristic morphological features, including (i) a convective core typically composed of one or more updraft regions with heavy, convective rain that translates through the freezing level and (ii) a horizontally spreading anvil, composed of glaciated and supercooled liquid hydrometeors, that may or may not be raining. We have found these and other morphological features to be readily identifiable in CloudSat profiles and have developed and implemented two algorithms to define such features within our data set in order to generate useful information about their spatial, thermodynamic, and radiative characteristics.

The first algorithm, described here, partitions deep convective cloud objects into upper anvil and lower pedestal regions (so that the anvil rests on the pedestal) (Figure 4a). A single deep convective cloud object, as defined by the criteria in section 2.2.1, may contain multiple convective core regions. We introduce the term pedestal, which encompasses everything below the anvil, for precision of terminology. The second algorithm, described in section 2.2.3, estimates the number of "convective cores" within each cloud object's pedestal.

The goal of the cloud object partitioning algorithm is to identify a cutoff height for each cloud object. All cloudy pixels above the cutoff height will be considered part of the anvil region and all cloudy pixels below the cutoff height will be considered part of the pedestal region. An object-by-object approach provides two advantages over one that applies a single height cutoff to all objects: first, it yields improved anvil property estimates by adjusting to each individual cloud objects' morphology; second, it yields a new metric, lower anvil height, that can be used to generate statistics about the lowest height at which detrainment occurs in various regimes.

The cloud object partitioning algorithm determines a pedestal-anvil cutoff height for each cloud object according to the profile of the number of cloudy pixels identified in each of the cloud object's vertical levels.

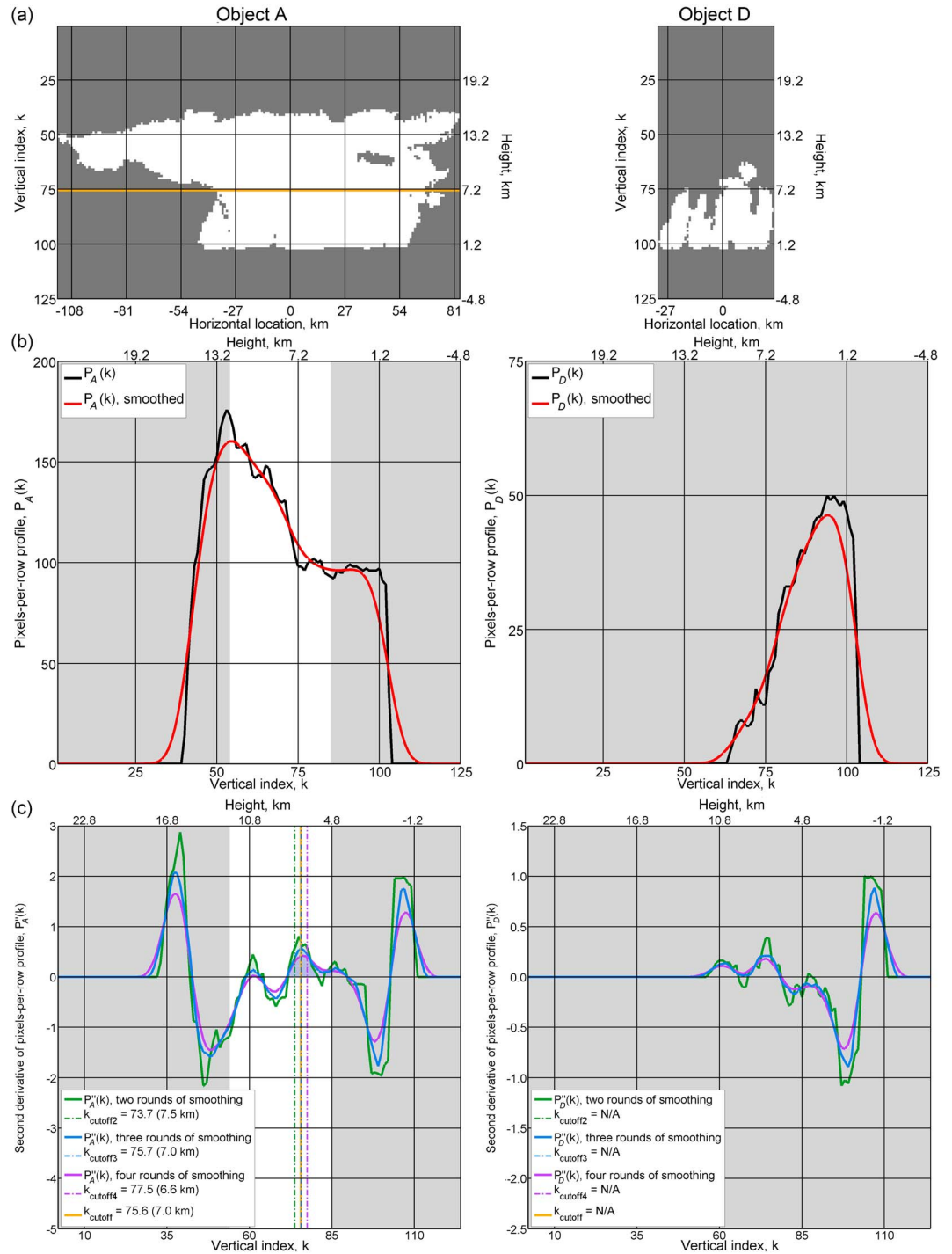


**Figure 4.** Illustration of cloud object partitioning algorithm for object A, for which an anvil is identified, and object D, for which no anvil is identified. (a) Images of objects A and D. (b) Cloudy-pixels-per-row profiles  $P_A(k)$  and  $P_D(k)$  before and after smoothing.  $P_A(k)$  becomes negative as anvil begins narrowing to pedestal, whereas  $P_D(k)$  does not become negative until cloud base. (c) As the anvil completes the transition to pedestal,  $P_A'(k)$  approaches zero, and  $P_A''(k)$  becomes positive. The partitioning algorithm identifies a cutoff by searching the unshaded region, starting where  $P_A'(k)$  becomes negative and ending at  $k=85$ , for regions where  $P_A''(k)$  is positive. The solid lines show the profile of width with various levels of smoothing and the dashed lines the corresponding cutoff height. The orange line illustrates the final cutoff height for the object in Figures 4a and 4c for object A. For object D, there exists no unshaded region to search, and so the algorithm does not identify a cutoff.

This metric captures characteristic changes in cloud width at different vertical levels. We define a cloudy-pixels-per-row profile  $P_n(k)$  for the  $n$ th object,

$$P_n(k) = \sum_{j_{n,k}} C(j, k), \quad (1)$$

where  $j_{n,k}$  are the horizontal indices contained in the  $k$ th vertical level of the  $n$ th cloud object. Figures 4a and 4b illustrates this process for objects A, for which an anvil is identified, and D, for which no anvil is identified. In Figure 4a, the binary cloud object is shown; in Figure 4b, the vertical profiles of  $P_A(k)$  and  $P_D(k)$  are shown. Note that the standard CloudSat vertical index increases with decreasing height; for example,  $k=80$  corresponds to an average height of 6 km, while  $k=105$  corresponds roughly to sea level. Inspection of the cloudy-pixels-per-row profiles corresponding to several mature deep convective cloud objects reveals a characteristic positive curvature in  $P_n(k)$ , or a dramatic increase in the *rate* of object widening with height, as anvil transitions to pedestal. In essence, the cloud object partitioning algorithm identifies the height at which this transition occurs by locating this characteristic curvature in  $P_n(k)$ . After computing  $P_n(k)$ , we smooth the profile three times by repeatedly applying a moving-average filter with a span of eight. Three passes leaves the characteristic shape of the profile while sufficiently eliminating undesirable noise which would otherwise trap our attempts to numerically find the cutoff height. The first and second derivatives with respect to index  $k$  of  $P_n(k)$ ,  $P_n'(k)$ , and  $P_n''(k)$ , respectively, are then computed. The cutoff index,  $k_{\text{cutoff}}$ , is determined by computing a weighted average of the indices  $k$  for which  $P_n''(k)$  is positive,

$$k_{\text{cutoff}} = \frac{\sum_{k=k_{\min}}^{k_{\max}} k \cdot P_n''(k) [P_n''(k) > 0]}{\sum_{k=k_{\min}}^{k_{\max}} P_n''(k) [P_n''(k) > 0]}, \quad (2)$$

where  $k_{\min}$  is the minimum vertical index such that  $P_n'(k) < 0$  and where  $k_{\max}$  equals 85 (see below). The Iverson brackets (square braces in equation (2)) obtain a value of one if the condition inside the brackets is true and zero otherwise. For example, the summation in equation (2) is conducted over the entire unshaded region of Figure 4c, but only the data from  $k=70$  to  $k=85$  contribute. The value of  $k_{\min}$  is chosen so that any detected positive curvature at upper levels coincides with narrowing from anvil to pedestal. The value of  $k_{\max}$  corresponds to a height of approximately 4.8 km and was chosen to prevent positive curvature in  $P_n(k)$  near cloud base from affecting the computed cutoff height. Note that for some cloud objects, such as object D,  $P_n(k)$  increases monotonically (i.e., the cloud only widens) as  $k$  increases from 1 to 85, which leaves  $k_{\min}$  undefined (hence the lack of unshaded region in the right-hand side of Figure 4c) and prevents the use of equation (2) to compute  $k_{\text{cutoff}}$ . By virtue of their lack of any narrowing from anvil to pedestal, these cloud objects are unlikely to have reached maturity (i.e., have a well-defined anvil) and are therefore removed from the data set.

Profile smoothness decreases with each level of differentiation, and we have observed that the amount of smoothing required to obtain useful  $P_n''(k)$  profiles varies among cloud objects. In order to account for this diversity, two additional calculations of the cutoff index are performed: one with two rounds of moving-average smoothing ( $k_{\text{cutoff}2}$ ) and one with four rounds of moving-average smoothing ( $k_{\text{cutoff}4}$ ). For these calculations,  $k_{\min}$  is still determined using the  $P_n'(k)$  profile calculated with three rounds of moving-average smoothing. If none of these calculations result in the cloud object's removal from the data set, we use these in addition to the previously computed cutoff index, which we will now call  $k_{\text{cutoff}3}$ , to compute a final cutoff index,

$$k_{\text{cutoff}} = \frac{k_{\text{cutoff}2} + 2 \cdot k_{\text{cutoff}3} + k_{\text{cutoff}4}}{4}. \quad (3)$$

All cloudy pixels with vertical index greater than  $k_{\text{cutoff}}$  are designated pedestal, and all cloudy pixels with vertical index less than or equal to  $k_{\text{cutoff}}$  are designated anvil. Subjectively from Figure 4, it can be seen that this method works. For object A, a subjective guess of the anvil cutoff height might be level 75. Equation (3) assesses that the level is 76 which is certainly consistent with the subjective guess. In fact, the cutoff algorithm exhibits remarkable skill compared to subjective analyses across a large number of objects.

### 2.2.3. Counting Convective Cores

After each cloud object is partitioned into its anvil and pedestal regions, a second algorithm is used to estimate the number of convective cores within the pedestal region of each cloud object. This is the stage of our analysis with potentially the least skill. In theory, convective cores would be best defined as regions of strong vertical ascent within cloud objects' pedestal regions [LeMone and Zipser, 1980]. However, neither the A-Train satellites nor any reanalysis data provide the high-resolution spatiotemporal vertical velocity information necessary to identify convective cores according to this definition. Instead, we use relative CloudSat-derived radar reflectivity as a proxy for comparative convective vigor and operationally define convective cores as, essentially, along-track local maxima in reflectivity. While radar reflectivity is an imperfect proxy for convective vigor, it has been found to be useful here in estimating the number of convective cores in a given cloud object's pedestal region, which is the sole objective of the core-counting algorithm. Use of such a reflectivity proxy is not without precedent [Houze, 1993; Yuter et al., 2005; Luo et al., 2008].

The core-counting algorithm examines the reflectivity profiles at the 15 lower vertical levels from  $k=85$  (approximately 4.8 km height) to  $k=99$  (approximately 1.4 km height). Each of these vertical levels will contain at least one cloudy pixel due to earlier filtering by vertical extent, and these vertical levels will all lie within the pedestal region due to the earlier restriction on cutoff height. We begin by obtaining a snapshot of radar reflectivity at vertical levels  $85 \leq k \leq 99$  and horizontal indices  $j_{\min} \leq j \leq j_{\max}$ , where  $j_{\min}$  and  $j_{\max}$  are the horizontal indices of the leftmost and rightmost cloudy pixels, respectively, present in vertical levels 85 through 99. The value of radar reflectivity at clear (noncloudy) pixels is set to  $-28$  dBZ, and the radar reflectivity snapshot is smoothed by twice convolving it with a  $2 \times 2$  pixel averaging filter, which adjusts the reflectivity at each pixel in dBZ units,  $Z(j,k)$ , based on the reflectivity values at neighboring pixels:

$$Z_{\text{smoothed}}(j, k) = \frac{4 \cdot Z(j, k) + 2 \cdot \sum Z_{\text{directly adjacent}} + \sum Z_{\text{diagonally adjacent}}}{16}. \quad (4)$$

The reflectivity snapshot may contain local reflectivity maxima that are associated with immature convective plumes rather than convective core regions that feed into the cloud object's anvil. As Figures 2 and 3 show, object A (green) contains one of these plumes just north of  $21^\circ\text{N}$  and object E contains two of these plumes just south of  $13^\circ\text{N}$ . In order to prevent these immature plumes from affecting the count of convective cores, we remove from the pedestal analysis any column within the cloud object that either contains no cloudy pixels with vertical index greater than or equal to 99 or contains more than three noncloudy pixels between vertical levels 66 and 99. In this way, continuous or near-continuous vertical coverage is ensured through about 9.4 km among columns that are included, which we term "valid" columns. We further remove any isolated sets (termed "islands") of three or fewer consecutive valid columns fitting the above criteria from the pedestal analysis. If no valid columns remain, we remove the cloud object from the data set. Object C is removed on this basis; this object is likely to be an immature plume convecting into a preexisting anvil. Unfortunately, this computationally necessary step sets an artificial minimum pedestal width ( $w_p$ , next section) of 4.3 km. Figure 5a highlights the reflectivity snapshot for valid columns of object A, for which the core-counting algorithm identifies eight cores.

The smoothed radar reflectivity field corresponding to each island of four or more consecutive valid columns is then examined in order to estimate the number of convective cores contained in the entire pedestal region. For each island, we follow the following procedure:

1. Locate maxima (including those occurring on pedestal edges) with reflectivity of at least 0 dBZ at each vertical level. If no local maxima meet this criterion at a given level, record a value of zero cores at that level. Maxima in object A meeting this criterion are indicated in white in Figure 5a and with white-filled triangles in Figure 5b.
2. If there are at least two maxima at a given level, count the number of nonedge local minima such that the difference between the reflectivity at the minimum and the maximum of the reflectivities at its adjacent maxima is at least 2.5 dBZ. Add the number of minima satisfying this criterion to the previously recorded value for the number of cores at that level. Minima in object A meeting this criterion are indicated in black in Figure 4b and with black-filled triangles in Figure 5b.
3. If a value of zero cores has been recorded at one or more levels, return to step 1 and decrease the reflectivity threshold for local maxima by 1 dBZ (down to a minimum of  $-10$  dBZ if necessary). This tuning

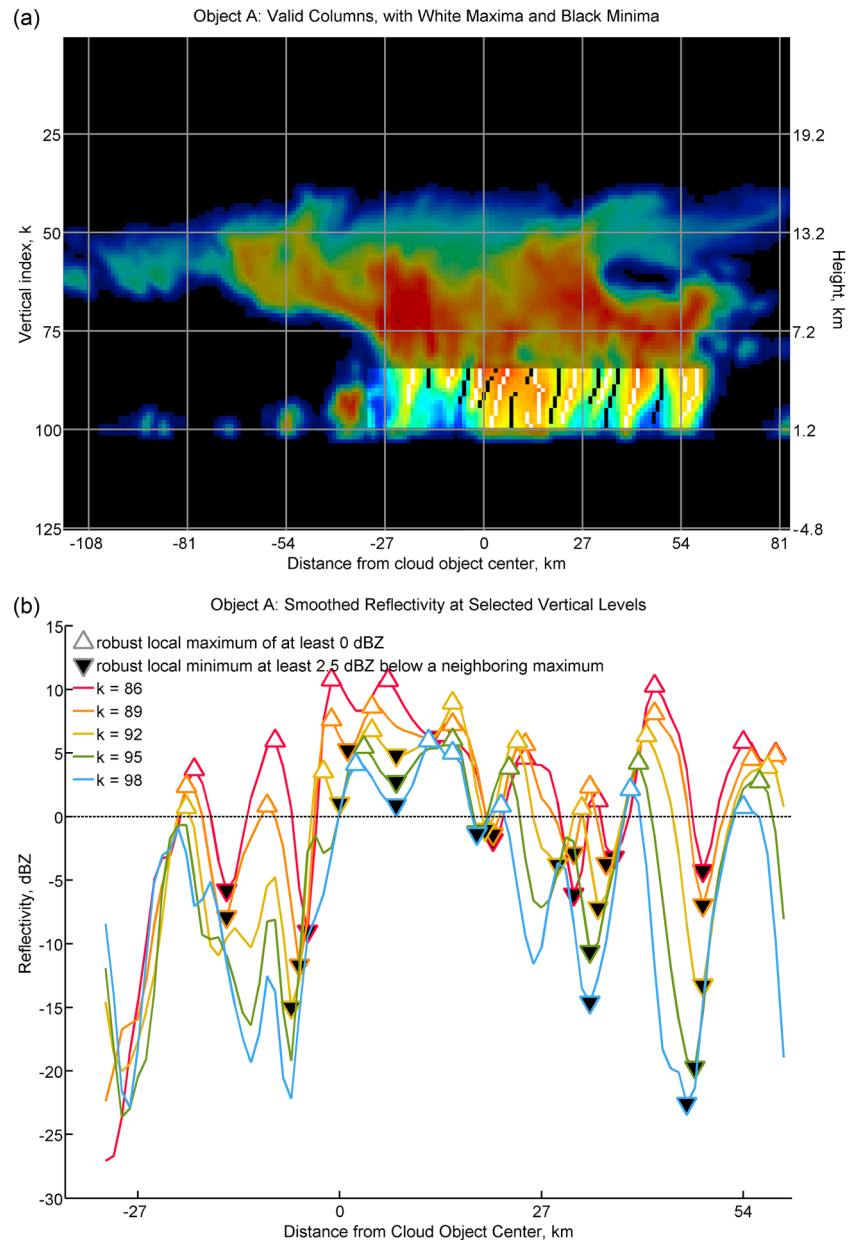


**Figure 5.** Illustration of core-counting algorithm for object A, for which eight cores are counted. (a) Reflectivity image of object A after smoothing is applied. Vertical levels 85 through 99 of valid columns are highlighted. The immature convective plume on the left edge of the pedestal is eliminated by column validity requirements. The robust local maxima and minima used to count cores are colored white and black, respectively. (b) Reflectivity at five vertical levels within the region highlighted in Figure 5a.

- of the reflectivity threshold allows us to account for varying amounts of attenuation while preventing weak local maxima from being counted as cores.
- Take the median of the number of cores recorded at each level, excluding levels for which no core was reported. Figure 5b illustrates how the number of cores recorded for object A varies with vertical level. If no cores are reported at any level, record a value of 1 so that each island is determined to contain at least one convective core.

The total number of convective cores in a given cloud object’s pedestal region is estimated by summing the numbers of convective cores identified within each island of valid columns. This final step is unnecessary

for object A, which has only one island of valid columns. For object A, we obtain an estimate of eight cores from the approach described. This estimate agrees reasonably well with the estimate of eight or nine cores that would be obtained subjectively. It should be reiterated that our core-counting algorithm is based on the assumption that the degree of inhomogeneity in the reflectivity field of the pedestal is indicative of the number of convective elements. As such, this algorithm is used to provide an order-of-magnitude estimate of the number of cores, rather than a precise measure of their location.

#### 2.2.4. Defining Morphological Attributes

Once likely deep convective cloud objects over tropical oceans have been identified and partitioned according to the methods delineated above, information on the morphology of cloud objects are recorded. In particular, we are interested in determining the characteristic pedestal width ( $w_p$ ), anvil width ( $w_a$ ), pedestal depth ( $D_p$ ), and anvil depth ( $D_a$ ). The height of cloud base ( $H_{cb}$ ), cloud top height ( $H_t$ ), and anvil-pedestal cutoff height ( $H_{cutoff}$ ) are also recorded. This choice of length scales and variable names in part follows that of *Bacmeister and Stephens* [2011]. Indeed, our definitions of  $H_{cb}$  and  $H_t$ , the heights of the lowest and highest pixels within a given cloud object, are identical to those of *Bacmeister and Stephens* [2011]. In order to compute  $H_{cutoff}$ , the average height corresponding to cutoff index  $k_{cutoff}$  (which is rarely an integer) is estimated by interpolating between the average heights of cloud object pixels at the vertical levels immediately above and below the cutoff. From these heights we calculate pedestal depth,

$$D_p = H_{cutoff} - H_{cb}, \quad (5)$$

and anvil depth,

$$D_a = H_t - H_{cutoff}. \quad (6)$$

We depart somewhat from *Bacmeister and Stephens* [2011] in our definitions of widths in order to capture the relationship between anvils and their corresponding convective cores in such a manner that only those pedestal regions that feed mass into the anvil are included while associated immature convection is excluded. Pedestal width ( $w_p$ ) is determined by multiplying the horizontal spacing, 1079 m, by the number of valid columns identified as in the previous section. In this way, columns corresponding to likely immature convection (as well as islands of three or fewer valid columns) are removed from the calculation. Anvil width ( $w_a$ ) is determined by multiplying the horizontal spacing by the number of columns containing at least one cloudy anvil pixel, as defined in section 2.2.2. Note that columns that were removed in the calculation of pedestal width are included in the calculation of anvil width, as well as in the calculations of the heights and depths discussed above. Finally, based on these widths, a detrainment index,  $I_d$ , is defined in the manner of *Bacmeister and Stephens* [2011],

$$I_d = \frac{w_a}{w_p}. \quad (7)$$

#### 2.2.5. Defining Environmental Characteristics

In addition to recording information about each cloud object's spatial attributes, information about the environment in which each cloud object resides is also recorded. Each cloud object is assigned a single latitude and longitude. These values are determined by averaging the latitudes and longitudes, respectively, of each of the cloud object's cloudy pixels. Further environmental information is taken from the ECMWF-AUX auxiliary CloudSat data product, which interpolates ECMWF state-variable data to CloudSat data bins [*Partain*, 2007]. The "skin\_temperature" field is commonly used to calculate an average sea surface temperature (SST) for each cloud object. Since we are particularly interested in the temperature of the water fueling the observed convection, this average is computed across the valid columns previously used to calculate pedestal width. ECMWF SST, the "Sea\_surface\_temperature" field, (mixed layer) values are also included in a similar way.

The ECMWF-AUX product provides information about temperature, pressure, and relative humidity at the bottom and top of each cloud object's anvil region. A lower anvil temperature is computed for each cloud object by averaging the analysis temperature values at pixels in the lowest vertical level within the anvil. Lower anvil pressure and relative humidity values are assigned similarly, with relative humidity calculated based on ECMWF-AUX "Temperature," "Pressure," and "Specific\_humidity" fields using the Goff-Gratch equation (<http://cires.colorado.edu/~voemel/vp.html>). Cloud top temperature is computed by averaging the temperature values at the top cloudy pixel of each anvil column. In order for a column to be included in

the average, its top cloudy pixel must have a vertical index  $k \leq 63$  (approximately 10.0 km height or greater). In this way, irrelevant temperatures atop immature convective plumes and shallow sections of anvil are omitted from the calculation of the average. Cloud top pressure is computed in a similar manner. In an effort to provide an environmental, clear air value, cloud top relative humidity is computed based on values two pixels (480 m) above the top of each column.

Lastly, anvil optical depth is estimated from the 2B-TAU [Polonsky *et al.*, 2008] product, and ice water content is taken from 2B-CWC-RVOD [Wood, 2008]. First, the layer optical depth and ice water content of anvil pixels are summed for each column to give a vertically integrated total optical depth and ice water path for that column's anvil pixels. Then, the mean and standard deviation of these column totals are recorded. For a sizeable number of anvil columns, layer optical depth values are missing from the raw data; for a smaller number, ice water content values are missing. These columns are not included in the calculation of these quantities, and we record the fraction of missing columns for each cloud object, which is sometimes large. From separate analyses assuming ice-only and liquid-only retrievals, the 2B-CWC-RVOD product assigns each point an ice water content and a liquid water content based on the ECMWF-AUX-derived temperature at that point. The product assigns the ice-only value for temperatures below  $-20^{\circ}\text{C}$ , the liquid-only value for temperatures above  $0^{\circ}\text{C}$ , and a linear combination of the two for temperatures between  $-20^{\circ}\text{C}$  and  $0^{\circ}\text{C}$ . For simplicity, our analyses make use only of the resulting ice water content field, "RVOD\_ice\_water\_content." Column total heating rates have been added from the 2B-FLXHR [L'Ecuyer *et al.*, 2008] product for all cloudy columns. Column rates are summed across all the columns of each object in order to produce a single value for each cloud object.

#### 2.2.6. Postprocessing Thresholding

The steps outlined thus far produce an initial data set containing approximately 26,000 deep convective tropical cloud objects over a 5 year period. The criteria for inclusion in this data set are intentionally permissive so as to include all cloud objects whose morphological and environmental attributes can be defined according to the methods outlined above. After this initial data set has been created, cloud objects can still be filtered according to geolocation, time of year, or any other morphological or environmental attribute. In the analyses to follow here, we only include cloud objects with  $H_t > 11$  km,  $I_d > 1.5$ , and  $298.75\text{ K} < \text{SST} < 303.75\text{ K}$ . These values allow us to target mature, deep convection over an SST range for which there are many objects. The additional restrictions reduce the size of the data set to approximately 22,000 cloud objects, a quantity more than sufficiently large to yield well-collapsed statistics.

#### 2.2.7. Composite Cloud Images

Composite cloud images are constructed as a means of visualizing the properties of subsets of cloud objects within our data set in the following way. We use classifications from the 2B-CLDCLASS cloud\_scenario to select a subset of our data. The cloudy pixels making up the convective pedestal regions that feed into the anvil and the cloudy pixels making up the anvil, are those classified as either cirrus (1), altostratus (2), or deep convection (8). Pixels we do not want to include for these simple composites are those classified either as altocumulus (3), stratocumulus (5), cumulus (6), or in rare cases, stratus (4). Figure 3c illustrates the relevance of the prior and irrelevance of the latter for object E. Young *et al.* [2013] show complimentary results. Thus, the first step in constructing composite cloud images is to eliminate pixels with a cloud\_scenario value other than 1, 2, or 8. The images are then aligned according to the average horizontal index of remaining cloudy pixels present in vertical levels 85 through 99. This step colocalizes the lower cloud pedestals. Each cloud object is then placed on a grid larger than the largest object with cloudy pixels given a value of 1 and clear pixels a value of 0. All the grids are then averaged together. Finally, a color scale is applied and the values of all pixels valued below 0.10 are set to zero (black) to accentuate the 0.10 contour. It is important to note that due to the alignment step of the compositing process and diversity of cloud object shapes, these plots always result in what appears to be a single-core-like object.

It is worth stating explicitly that these composites are used only for visualization purposes. While they provide very insightful qualitative comparisons, they are not intended to provide any quantitative information. Composite cloud images are, in essence, averages of cloud object binary images such as those shown in Figure 4a, or, equivalently, averages of the binary fields  $C(j,k)$  corresponding to each cloud object. The vast nature of our data set allows statistically meaningful composites to be constructed from subsets containing as little as two percent of the total data. Here objects are binned according to lower anvil height in order to provide validation of the anvil-pedestal cutoff algorithm; later, cloud objects are binned according to sea surface temperature in order to evaluate proposed cloud-SST dependencies.

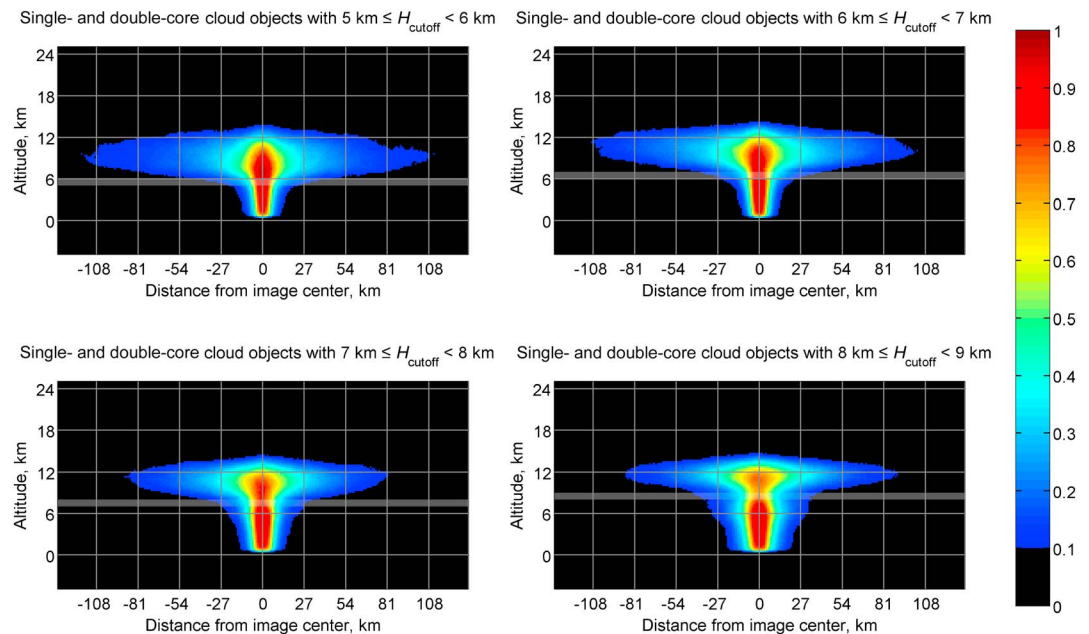


**Figure 6.** Composite cloud images of single- and double-core cloud objects for four ranges (highlighted on the images) of lower anvil heights. The shading represents the fraction of clouds that would overlap if cloud base centers were collocated.

Figure 6 shows composite images generated from single-core and double-core clouds (as determined by the core-counting algorithm) for various ranges of lower anvil heights (as determined by the pedestal-anvil cutoff algorithm). Each image is made up of approximately 1800 cloud objects. The composite anvils do, in fact, appear to detrain higher in the cloud as the cutoff height is increased. Furthermore, each binned cutoff height (highlighted) appears to match the height of the transition from pedestal to anvil in its corresponding composite image. Finally, it should be noted that the concave structure at the highest percentages in Figure 6d near the cutoff height is due primarily to increasing inhomogeneity in cloud object structure with increasing cutoff height. Figure 6 therefore exemplifies the utility of this visualization tool, one of simple qualitative assessment.

### 3. Data Validation

This section includes a discussion of the spatial and temporal frequency distributions of cloud object occurrence (i.e., cloud object number densities). These distributions will be compared to results that have been obtained in previous studies. It is noted that prior studies have examined cloud fraction, which is

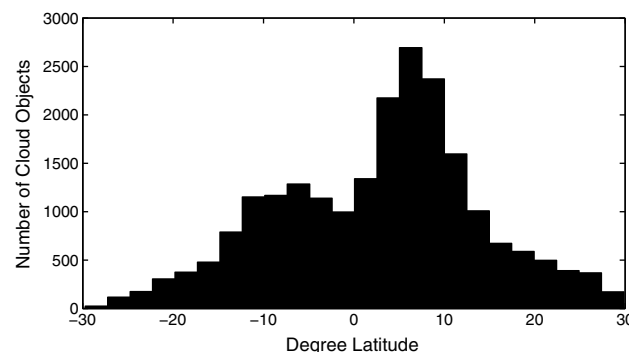


**Figure 7.** Population of deep convective cloud objects binned by latitude over the 5 years of the data set. Bins are 2.5° wide.

not a precisely equivalent metric to frequency of deep convective cloud object occurrence since the objects used herein are very specifically selected. Nevertheless, it will be shown that the data set developed in the previous section has realistic distributions of cloud objects across space and time, and it will be suggested that the data set does not need additional spatial or temporal thresholds. While subtle differences between the developed data set and past results do occasionally arise, it is evident that none of these are sufficiently significant enough to affect the conclusions drawn in section 4.

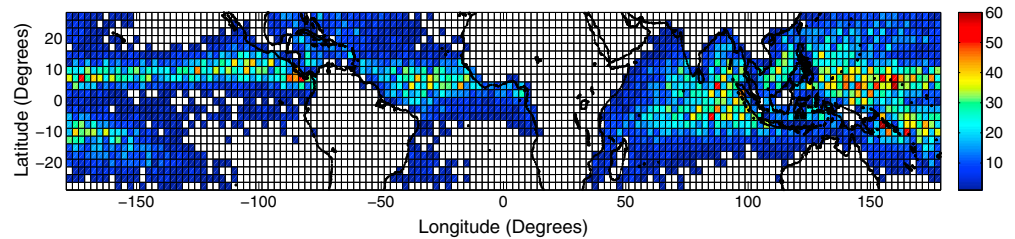


**Figure 8.** Spatial counts of cloud objects in  $2.5^\circ \times 2.5^\circ$  bins for the entire data set.

### 3.1. Geospatial Statistics

Various spatial frequency distributions of cloud objects are detailed in this section. Some of the first results are similar to those of *Sassen et al.* [2009] who used 2 years of combined CloudSat and CALIPSO data, but the results shown here arise from a very different data set.

First, the frequency distributions of object centers by latitude is presented in Figure 7. The figure illustrates the number of cloud objects deemed to center within a certain  $2.5^\circ$  latitude bin. Although, this is not a plot of cloud fraction, common features of cloud fraction plots are exhibited including local maxima at  $\sim 8^\circ\text{S}$  and  $\sim 8^\circ\text{N}$  (due to the Intertropical Convergence Zone (ITCZ)), a local minimum at the equator, and a steady decrease in magnitude toward the poleward extent of the tropics. The figure looks similar to previously reported results from both recent global models and observations [*Sassen et al.*, 2009; *Probst et al.*, 2012]. Regional binning and analysis of cloud objects (not shown) indicates that mean cloud sizes are similar among regions. This result agrees with the similarities between the cloud object occurrences presented in Figure 7 and the International Satellite Cloud Climatology Project cloud fraction [*Probst et al.*, 2012], which implies that coverage per cloud object is roughly uniform and therefore that cloud size is similar across regions.

A global, two-dimensional occurrence frequency plot is shown in Figure 8 with  $2.5^\circ \times 2.5^\circ$  bins. It can be seen that the only ocean regions completely lacking deep tropical convective cloud objects are over the stratocumulus decks off of the western side of continents [*Wood*, 2012]. While other nonstratocumulus regions may exhibit local minima, they are not bereft of deep convection. Regions frequently within the ITCZ tend to exhibit the highest number density of deep convective cloud objects. Other local maxima in cloud objects exist in the Caribbean and northern tropical Atlantic, the South Pacific Convergence Zone, the Bay of Bengal, the northern tropical Pacific especially just west of Panama, and the southwestern tropical Atlantic. It is therefore evident that deep convective cloud object occurrence is fairly ubiquitous.

Figure 8 is suggestive of the elimination of cloud objects due to overlaying of land or intersection with the tropical boundary by the methodology developed. In several places, islands (e.g., Hawaii, Indonesia, or Hispaniola) or continent boundaries (e.g., the Yucatan or parts of Australia) can be seen to correlate to local minima or zeros in cloud object count over the ocean near the respective location even though there is no physical reason to expect such a minimum. There is also an interesting lack of cloud objects in the central Pacific along the equator between  $100^\circ\text{W}$  and  $130^\circ\text{W}$ . This result appears to be the consequence of two factors. The first is a climatological lack of clouds in this region [*Liao et al.*, 1995]. But this probably cannot explain the total lack of cloud objects in some latitude-longitude bins. It could illustrate a problem with the standard thresholds used in this study, although easing some of these thresholds did not generate many more cloud objects in this region. Alternatively, this lack of cloud objects may illustrate a daily sampling bias of CloudSat by which clouds are not vertically developed in this region at 1330 local standard time. Including the nighttime overpass in the data set could answer this question although *Sassen et al.* [2009] did not notice significant differences between night and day in 2 years of data over the East Pacific.

### 3.2. Temporal Statistics

The analysis in this section will serve to complement the spatial analysis in the previous one by describing whether the methodology developed above introduces any significant temporal biases. Regionally, tropical convection is observed to undergo significant variability over the course of the year [*Sabin et al.*, 2013]. However, when the tropical oceans are examined as a whole, clouds often do not exhibit much of a seasonal cycle [e.g., *Christian et al.*, 2003; *Stubenrauch et al.*, 2006]. To confirm this in our data set, Figure 9 shows the population of cloud objects divided into 5 day bins. Day 366 of 2008 has been excluded for the

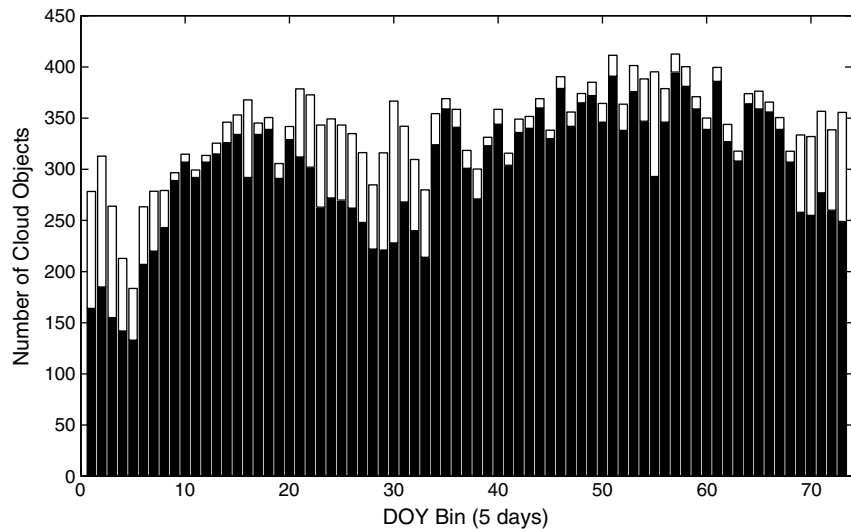


**Figure 9.** Temporal population density of cloud objects. Bins are 5 days wide and begin on 1 January. White bars represent an artificial addition of data to account for CloudSat operational date nonuniformity and other missing data. Data include Northern and Southern Hemisphere cloud objects.

sake of symmetry, and data from both the Northern and Southern Hemispheres are included. Actual data from 2006 day 166 to 2011 day 107 are in black bars. White bars show an attempt to account for missing data resulting from CloudSat downtime or missing data by adding an artificial number of objects to each day based on the ratio of observations occurring on that day to the highest number of occurrences on any day (day 225, day of year bin 45). These additions are done to facilitate comparisons using this figure and do not impact the data set in any way. The primary implication drawn from Figure 9 is a lack of any strong, tropics-wide yearly cycle in the frequency of cloud object occurrence. The second is that a local, temporal minimum does exist near the beginning of the calendar year. This signal exists across all basins and in both the Northern and Southern Hemispheres. Speculatively, it may be a tropical response to the seasonal progression of the Hadley cell [Mitchell and Wallace, 1992], a statistical anomaly, or some minor methodological bias. In the event that it is real, it could imply that during these weeks, clouds are more efficient rain producers per cloud object given global moisture constraints. Perhaps indicative of such an idea is that clouds are computed to be  $\sim 10\%$  wider during the first 25 days of the year than the final 340 which could imply weaker entrainment, but we find little additional evidence to suggest this. Or, the explanation might be that a large population is somehow eluding the database through the selection criteria or, as stated above, by diurnal cycle.

The results in sections 3.1 and 3.2 detail the spatiotemporal occurrence of cloud objects and demonstrate that our intentionally inclusive data set is not biased by such inclusions. Subsetting by time or space could have uses but does not seem to be necessary to understand the physics of deep convective cloud objects. These facts should help to address concerns that examining cloud objects across the tropics with no meteorological subsetting might not be justified. The database will now be used to examine anvil-SST relationships.

#### 4. Anvil-SST Morphological Trends

The simplest cloud anvil-SST response to investigate with the new methodology is the proposed Iris Hypothesis [Lindzen *et al.*, 2001] which stipulates that anvil areal extent should decrease with increasing SST. Critically, CloudSat retrievals provide no means of evaluating cloud area; they only provide along-track length information. However, if the mean of many clouds can be assumed to be morphologically isotropic in the horizontal as discussed above, then cloud anvil width can be thought of as a diameter from which a horizontal anvil area can be computed. The results of M. R. Igel and S. C. van den Heever (Deep convective cloud morphology as observed by CloudSat, submitted to *Journal of Atmospheric Sciences*, 2014) indicate this may not be a bad assumption as they suggest that even though individual deep convective clouds may not be circular, only the most oblong anvils may be misleadingly measured by CloudSat. This result, combined with the

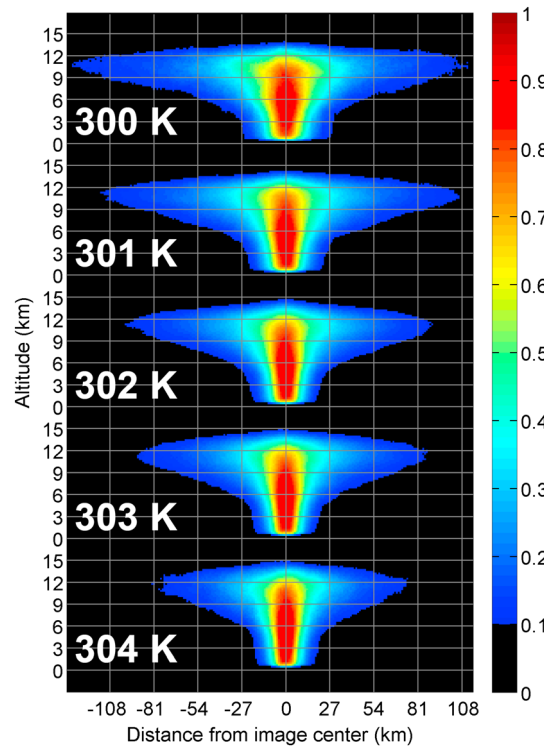


**Figure 10.** Fraction of cloud objects at each listed SST that would overlap at a certain grid point if all cloud centers were collocated. The magnitude indicates the fraction of clouds with cloudiness at each pixel relative to its pedestal base center. This figure is only to be used as a visualization aid. It shows that anvils narrow and rise with increasing SSTs.

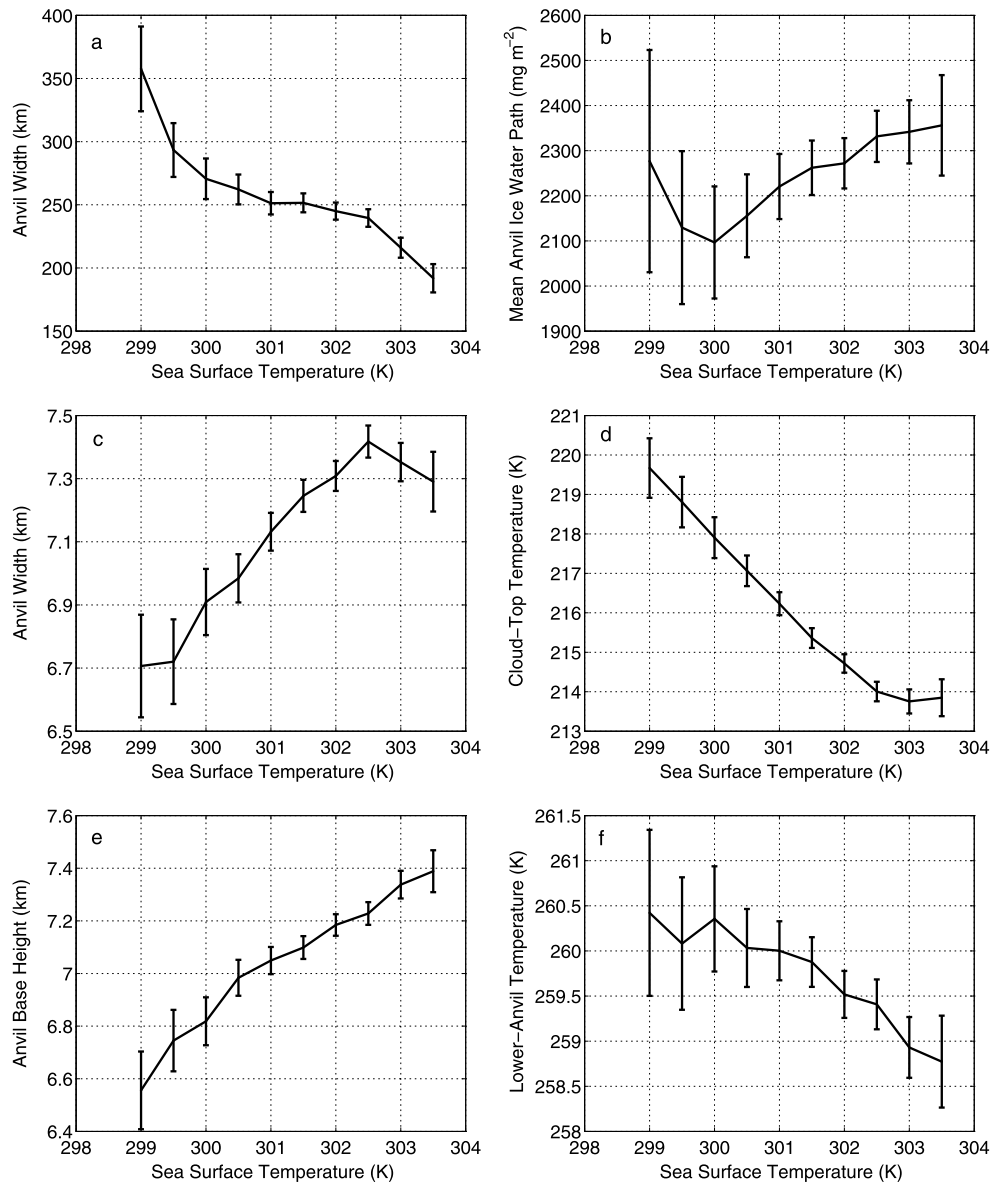
near symmetry of the cloud object composites in Figure 10, indicates that isotropicity is not an unreasonable assumption. While not wholly unreasonable, anvils are sometimes observed to orient in the zonal direction with the prevailing wind shear. In these cases, and indeed for all cases of noncircular anvils, the measured anvil width will be less than the true maximum value.

In Figure 11a, anvil width can be seen to decrease with increasing SST for SSTs over which we might hope to limit the influence of mean vertical motion [Lau *et al.*, 1997]. Also, in Figure 10, it is evident that anvils get narrower with increasing SST for any given overlap fraction. This result would imply an Iris-type response in nature. A plot of mean total anvil ice water content (not shown) broadly confirms this as it shows total ice content decreasing across the range of SSTs by ~40%. The number of objects in each SST bin are listed in Table 1. It will be noted that in Lindzen *et al.* [2001] the smaller anvils are proposed to result from an increase in precipitation efficiency; that is, increased rainout is thought to remove water mass from the cloud that would otherwise enhance anvils. If reflectivity over 0 dBZ is broadly thought of as indicating precipitation from CloudSat [Haynes *et al.*, 2009] with higher values indicating more intense precipitation, then examination of reflectivity structures within cloud objects (not shown) suggests deeper and more

intense rain shafts as SSTs increase. The increased depth of rain could also be inferred from Figure 10 although this figure includes no indication of actual reflectivity values. Of course, higher rain rates do not necessarily imply greater precipitation efficiency. However, given the trends in reflectivity, it is impossible to rule out an increase in precipitation efficiency as a possible mechanism. In Lindzen *et al.* [2001], pedestal area was assumed to remain constant as SSTs warmed while the anvil was proposed to wither. This is not the response observed here. The new data show that pedestal sizes decrease with increasing SST.

Next, the existence of a Thermostat-type response [Ramanathan and Collins, 1991] in these data will be assessed. Fundamentally, the Thermostat Hypothesis proposes that rising SSTs will result in more reflective anvil clouds through an increase in the total anvil water (likely, ice) mass. If all in-cloud-particle optical extinction properties are the same, this increase in mass would be observed correctly by measuring an increase in optical depth. Optical depth values, though, are frequently not successfully retrieved, so proxy data are required. Figure 11b shows that the mean CloudSat-derived anvil ice path increases with SST above 300 K, although it exhibits very little total trend between 298 K and 304 K. However, as Figure 11c demonstrates, anvil physical depth (the difference between cloud top height and anvil base height [i.e., the cutoff height]) increases with increasing SST. The results presented here are interpreted as supporting a Thermostat-like response. Physically thicker anvils and weakly increasing ice path of anvils above 300 K SSTs should be more reflective in that manner proposed by Ramanathan and Collins [1991].

Finally, the existence of a FAT-type [Hartmann and Larson, 2002] response to surface warming will be assessed. Counter to the FAT Hypothesis, Figure 11d indicates that cloud top environmental temperature decreases with increasing SST. The cooling occurs at approximately 1.6 K/K for SSTs between 299 K and 302.5 K. However, such a trend cannot rule out a FAT-type response. The cooling does appear to be robust (statistically at least) and has been suggested as a response to warming SSTs before from studies using different methods [Igel, 2011, Singh and O’Gorman, 2013]. It deserves some consideration. It is evident from



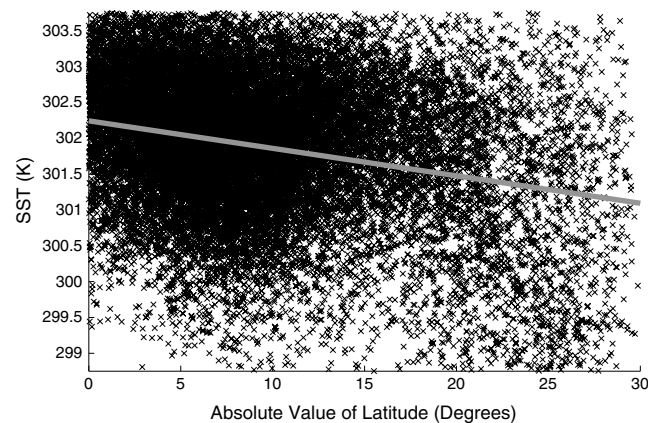
**Figure 11.** (a) Binned mean anvil widths (as a function of SST with confidence intervals in vertical bars), (b) Anvil ice water path, (c) Physical mean anvil depth, (d) ECMWF analysis temperature at the level of cloud top, (e) Anvil base height, and (f) ECMWF analysis temperature at the level of anvil base. Error bars indicate 95% confidence intervals for the mean in each SST bin.

Figure 10 that deep convection tends to get taller at a high enough rate as a function of SST that it produces cooler cloud top environmental temperatures in the level-by-level warmer atmosphere (at least in the mean). Taller (i.e., cooler) convective cells tend on average to be more vigorous than shorter (i.e., warmer) clouds. Thus, the cooler cloud top temperatures observed here are primarily indicative of more intense convection with

increasing SST—a result that perhaps is unsurprising. It is likely that FAT/PHAT mechanisms are more relevant in the former case than they are here as they rely on equilibrium arguments. And it should be noted that this analysis is limited by the coarse spatial resolution of ECMWF reanalysis data appended to the CloudSat data

**Table 1.** The Number of Cloud Objects in Each SST Bin in Figure 11

SST (K)	Number of Objects	SST (K)	Number of Objects
299	323	301.5	3968
299.5	499	302	4896
300	835	302.5	4739
300.5	1515	303	3282
301	2689	303.5	1437



**Figure 12.** Scatter of cloud objects occurrences by the magnitude of latitude and SST. The gray line shows the simple least squares fit to the cloud of data as a function of latitude.

“lower anvil” refers to the anvil-pedestal cutoff height,  $H_{\text{cutoff}}$ , as defined in section 2.2.4. As Figure 11e shows, mean anvil base height tends to rise with SST warming at a rate of  $0.15 \text{ km K}^{-1}$ . The reciprocal of this value, which gives the equivalent cloud base-SST lapse rate, is  $6.7 \text{ K km}^{-1}$ . The similarity between this lapse rate and the moist adiabatic lapse rate of  $6.5 \text{ K km}^{-1}$  (the typical lapse rate near tropical convection) suggests that this height rise is related to temperature. Specifically, the implication is that anvil bases rise approximately isothermally with surface warming. Figure 11f illustrates the same implied FLAT response by showing the ECMWF temperature at anvil base height. Despite the small change in the temperature of anvil base, the use of the term “fixed” is still appropriate given that the change in temperature should have a negligible radiative forcing. This reanalysis-derived temperature is environmental and is only approximately relevant for in-cloud temperature. It is also noted that due to processes such as ice particle sedimentation, a given cloud’s lower anvil height can be expected to vary over the course of a cloud’s lifetime [Yuan and Houze, 2010]. Implicit in this discussion is the assumption that CloudSat is sampling clouds across a representative set of lifecycle stages at all SSTs. Further work is necessary to evaluate the validity of this assumption and to assess whether the FLAT response can be reproduced in other contexts, such as numerical modeling experiments.

But, why should a FLAT response exist? Anvil-edge structure is dictated by a variety of diabatic processes: among them, radiation, evaporation/sublimation, and turbulent mixing. All three depend on temperature: radiation through the Stefan-Boltzmann law, evaporation/sublimation through the Clausius-Clapeyron relationship, and turbulence through changes in density if shear is low. The latter two mechanisms rely primarily upon pressure and temperature variations in the vertical. So it would seem reasonable to suggest that temperature dictates many anvil processes at the interface with clear air. For the lower anvil boundary, it is possible to imagine a first-order balance between warming from upwelling longwave radiation, which, in the moist tropics especially, is a function both of surface temperature and temperature at levels below cloud, and cooling from downwelling longwave radiation and evaporation/sublimation. This balance could conceivably occur at some temperature level in the atmosphere. If an anvil base is too warm, it would evaporate and cool until it reaches the desired temperature balance at the cooler level. This level would be approximately independent of surface temperature and would dictate where the lower boundary of the anvil would exist in equilibrium. As a result, mean anvil base temperature would remain approximately constant across meteorological or surface states in the tropics. It could also be that the anvil base is constrained by the mesoscale flow that tends to organize a dry inflow just above the melting level from clear air regions into deep convection [Posselt et al., 2008].

It has been shown before that potentially many convolving issues arise when analyzing cloud trends as a function of SST [e.g., Hartmann and Michelsen, 1993; Lau et al., 1997; Bony et al., 1997]. The present study is immune to some, but not all, of the complications arising from the correlation between time averaged SST and large-scale circulation due to the tropics-wide distribution of cloud objects in each SST bin as a result of the use of instantaneous SSTs. Figure 12 shows the distribution of cloud objects as a function of SST and latitude. Cloud objects exist in all SST bins at all latitudes  $30^{\circ}\text{S}$ – $30^{\circ}\text{N}$ . This ensures sampling in any SST bin

granules. The recent results of Chae and Sherwood [2010] implicate high-altitude processes as being important for the precise anvil temperature. It is critical to note that the physical arguments concerning FAT [Hartmann and Larson, 2002] are relevant to all high clouds emanating from deep convection. The clouds included in this data set are composed of a limited subset of all of these possible clouds, which may be influencing the precise trend in top temperature.

To conclude this section, a new cloud response to SST warming, the Fixed Lower Anvil Temperature (FLAT) Hypothesis, is proposed. The phrase

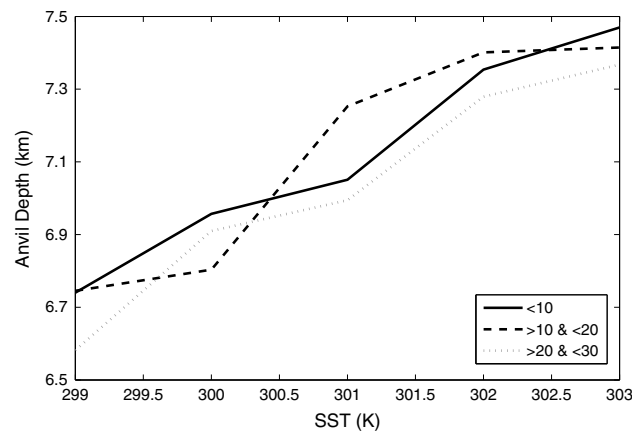


**Figure 13.** An example of the randomly resampled data wherein each  $10^\circ$  latitude bin and each 0.5 K SST bin is artificially limited to have the same number of samples. This figure shows the trend in anvil depth as a function of SST (as in Figure 3c) for the three latitude bins.

from within the climatological Hadley Cell ascent and descent regions. Figure 12 shows that the difference in mean SST between the equator and  $30^\circ$  is on the order of  $\sim 1$  K. This result is in contrast to the mean difference (in latitude) of monthly mean SST which is on the order of  $\sim 10$  K. This contrast implies latitude (large-scale circulation) and SST are much more independent in this data set than they are when clear sky is included. With the above responses in mind and in a final effort to ensure robustness of the data, the data have also been subsampled and reanalyzed to ensure that the trends presented hold regardless of large-scale flow regime and with a consistent number of cloud objects in each SST-latitude bin. Latitude is used as a modest proxy for large-scale flow. Data are resampled whereby equal numbers of data are randomly selected from within  $10^\circ$  latitude  $\times$  0.5 K bins. The trends are then reassessed with the new, limited data. Figure 13 shows one such sample of the data. It implies that the trend of increasing anvil depth with SST exists regardless of the latitude bin used. None of the trends shown in Figure 11 is ruled out by multiple random iterations of Figure 13. This type of figure was also created to compare trends with SST in both large-scale midlevel ascent and descent regimes as measured by ECMWF reanalysis 500 hPa pressure velocity. The trends with respect to SST did not change regardless of midlevel vertical ascent or descent.

## 5. Conclusions

A methodology to divide CloudSat data into individual cloudy regions (termed cloud objects) that exhibit certain shape and internal characteristics has been developed. Cloud objects are defined to be deep convection based on height, CloudSat cloud-type identification, and contiguity. A method for separating the cloud object into anvil and pedestal (on which the anvil sits) regions was developed. This method relied on a characteristic change in the vertical gradient of horizontal width. Additionally, an attempt was made to count the number of convective cores within each pedestal region, with some success. A composite image technique was also introduced. The population of cloud objects was shown to exhibit minimal potential bias in their distribution in space or time.

The derived cloud object data were used to analyze the dependence of anvil morphology on SST. Based on the analysis presented, we hypothesize that the various cloud-SST dependencies discussed function in the following synergistic manner. If FAT (Figure 12d) and FLAT (Figures 11e and 11f) can be assumed logically to be the most likely mechanisms occurring in the real atmosphere, then anvil clouds are left with strong upper and lower boundary conditions. Again, this is true insofar as both of these mechanisms are likely to be only first-order accurate. These hypotheses rely on temperature and seem to occur due to potentially strong physical constraints. The FAT in particular has shown robustness to past analysis despite the uncertainty here. The profile of temperature is relatively well constrained in the tropics [Meehl *et al.*, 2007; Igel *et al.*, 2014]. It is generally thought that, the tropical temperature profile is dictated by the moist adiabat which is a function of surface conditions (like those measured here). In conditions with a warmer surface, the moist adiabat is steeper due to the nonlinearity of the Clausius-Clapeyron relationship. This means that the temperature levels of the anvil base and anvil top, as dictated by the FLAT and FAT mechanisms, respectively, are farther apart in a warmer atmosphere. Consequently, anvils should become deeper if their base and top temperatures are constant. This response is essentially a Thermostat. It is also conceivable that if anvils become sufficiently deep in response to surface warming, and assuming only moderate changes in total detraining mass or volume, an Iris-type response might also occur, especially since anvils are much wider than they are tall. The assumption of constant detraining is certainly questionable, but the mean cross-

sectional area of anvils in the cloud object data do not exhibit a statistically significant trend from the 299.5 K to the 302.5 K bins and varies by only 30% across the entire range while the anvil width varies by 45% and continuously across the SST range. Total anvil ice path varies even less: 10% and 38%, respectively.

It is noted explicitly that these methods are only relevant to the mean of an ensemble of many cloud objects. Any cloud-climate response discussed herein should not be assumed to be at work for any individual cloud. The methodology relies on the assumption of strong statistical significance achieved through binning and averaging. Furthermore, the physical mechanisms behind the cloud responses to warming are thought of only in an equilibrium sense and often do not imply anything specific about an individual object. The climate, though, inherently depends on the ensemble mean of these responses. Ultimately then, cloud object methods are ideal tools with which to study the cloud-climate problem and their use in the future is encouraged. Future works will examine sensitivity tests to environmental characteristics (including SST) and cloud-resolving modeling simulation and will confirm this conclusion.

### Acknowledgments

Portions of this work were supported by NASA through CloudSat grant 5–319160 and an AMS graduate fellowship. Portions of this work have also been supported by the National Science Foundation Science and Technology Center for Multi-Scale Modeling of Atmospheric Processes, managed by Colorado State University under cooperative agreement No. ATM-0425247. The data used in this study can be obtained from the CloudSat Data Processing Center. The cloud object database used in this study can be obtained by contacting M. Igel at mattigel@atmos.colostate.edu. The authors would like to thank the anonymous reviewers who helped to improve this manuscript.

### References

- Bacmeister, J. T., and G. L. Stephens (2011), Spatial statistics of likely convective clouds in CloudSat data, *J. Geophys. Res.*, *116*, D04104, doi:10.1029/2010JD014444.
- Behrangi, A., T. Kubar, and B. Lambrigtsen (2012), Phenomenological description of tropical clouds using *CloudSat* cloud classification, *Mon. Weather Rev.*, *140*, doi:10.1175/MWR-D-11-00247.1.
- Bony, S., K.-M. Lau, and Y. C. Sud (1997), Sea surface temperature and large-scale circulation influences on tropical greenhouse effect and cloud radiative forcing, *J. Clim.*, *10*(8), 2055–2077.
- Bony, S., et al. (2006), How well do we understand and evaluate climate change feedback processes?, *J. Clim.*, *19*, 3445–3482.
- Chae, J. H., and S. C. Sherwood (2010), Insights into cloud-top height and dynamics from the seasonal cycle of cloud-top heights observed by MISR in the West Pacific, *J. Clim.*, *23*, 248–261.
- Christian, H. J., et al. (2003), Global frequency and distribution of lightning as observed from space by the Optical Transient Detector, *J. Geophys. Res.*, *108*(D1), 4005, doi:10.1029/2002JD002347.
- Del Genio, A. D., and W. Kovari (2002), Climatic properties of tropical precipitating convection under varying environmental conditions, *J. Clim.*, *15*, 2597–2615.
- Dias, J., S. N. Tulich, and G. N. Kiladis (2012), An object-based approach to assessing the organization of tropical convection, *J. Atmos. Sci.*, *69*(8), 2488–2504, doi:10.1175/JAS-D-11-0293.1.
- Harrop, B. E., and D. L. Hartmann (2012), Testing the role of radiation in determining tropical cloud-top temperature, *J. Clim.*, *25*, 5731–5747.
- Hartmann, D. L., and K. Larson (2002), An important constraint on tropical cloud-climate feedback, *Geophys. Res. Lett.*, *29*(20), 1951, doi:10.1029/2002GL015835.
- Hartmann, D. L., and M. L. Michelsen (1993), Large-scale effects on the regulation of tropical sea surface temperature, *J. Clim.*, *6*, 2049–2062.
- Haynes, J. M., and G. L. Stephens (2007), Tropical oceanic cloudiness and the incidence of precipitation: Early results from *CloudSat*, *Geophys. Res. Lett.*, *34*, L09811, doi:10.1029/2007GL029335.
- Haynes, J. M., T. S. L'Ecuyer, G. L. Stephens, S. D. Miller, C. Mitrescu, N. B. Wood, and S. Tanelli (2009), Rainfall retrieval over the ocean with spaceborne W-band radar, *J. Geophys. Res.*, *114*, D00A22, doi:10.1029/2008JD009973.
- Houze, R. A., Jr. (1993), *Cloud Dynamics*, 573 pp., Academic Press, San Diego, Calif.
- Igel, M. R. (2011), A tropical radiation and cloud system feedback modulated by sea surface temperatures, Masters thesis, 79 pp., Colo. State Univ., Fort Collins.
- Igel, M. R., S. C. van den Heever, G. L. Stephens, and D. J. Posselt (2014), Convective-scale responses of a large-domain, modeled tropical environment to surface warming, *Q. J. R. Meteorol. Soc.*, *140*, doi:10.1002/qj.2230.
- Kuang, Z., and D. L. Hartmann (2007), Testing the fixed anvil temperature hypothesis in a cloud-resolving model, *J. Clim.*, *20*, 2051–2057.
- Lau, K.-M., H.-T. Wu, and S. Bony (1997), The role of large-scale atmospheric circulation in the relationship between tropical convection and sea surface temperature, *J. Clim.*, *10*, 381–392.
- Lebsock, M. D., C. Kummerow, and G. L. Stephens (2010), An observed tropical oceanic radiative-convective cloud feedback, *J. Clim.*, *23*, 2065–2078.
- L'Ecuyer, T. S., N. B. Wood, T. Haladay, G. L. Stephens, and P. W. Stackhouse Jr. (2008), Impact of clouds on atmospheric heating based on the R04 *CloudSat* fluxes and heating rates data set, *J. Geophys. Res.*, *113*, D00A15, doi:10.1029/2008JD009951.
- LeMone, M. A., and E. J. Zipser (1980), Cumulonimbus vertical velocity events in GATE. Part I: Diameter, intensity and mass flux, *J. Atmos. Sci.*, *37*, 2444–2457.
- Li, Y., P. Yang, G. R. North, and A. Dessler (2012), Test of the fixed anvil temperature hypothesis, *J. Atmos. Sci.*, *69*, 2317–2328.
- Liao, X., W. B. Rossow, and D. Rind (1995), Comparison between SAGE II and ISCCP high-level clouds 1. Global and zonal mean cloud amounts, *J. Geophys. Res.*, *100*, 1121–1135, doi:10.1029/94JD02429.
- Lin, B., T. Wong, B. A. Wielicki, and Y. Hu (2004), Examination of the decadal tropical erbs nonscanner radiation data for the Iris Hypothesis, *J. Clim.*, *17*, 1239–1246.
- Lindzen, R. S., M.-D. Chou, and A. Y. Hou (2001), Does the Earth have an adaptive infrared Iris?, *Bull. Am. Meteorol. Soc.*, *82*, 417–432.
- Liou, K.-N. (1996), Influence of cirrus clouds on weather and climate processes: A global perspective, *Mon. Weather Rev.*, *114*, 1167–1199.
- Lloyd, J., E. Guilyardi, and H. Weller (2012), The role of atmosphere feedbacks during ENSO in the CMIP3 models. Part III: The shortwave flux feedback, *J. Clim.*, *25*, 4275–4293.
- Luo, Z., G. Y. Liu, and G. L. Stephens (2008), *CloudSat* adding new insight into tropical penetrating convection, *Geophys. Res. Lett.*, *35*, L19819, doi:10.1029/2008GL035330.
- Mace, G. (2006), Level2 GEOPROF product process description and interface control document algorithm version 5.3., *CIRA Tech. Rep. 5.3*, 42 pp., Colo. State Univ., Fort Collins.

- Manabe, S., and R. F. Strickler (1964), Thermal equilibrium of the atmosphere with a convective adjustment, *J. Atmos. Sci.*, *21*, 361–385.
- Meehl, G. A., et al. (2007), Global climate projections, in *Climate Change 2007: The Physical Science Basis. Contribution of Working Group I to the Fourth Assessment Report of the Intergovernmental Panel on Climate Change*, edited by S. Solomon et al., pp. 747–845, Cambridge Univ. Press, Cambridge, U. K., and New York.
- Mitchell, T. P., and J. M. Wallace (1992), The annual cycle in equatorial convection and sea surface temperature, *J. Clim.*, *5*, 1140–1156.
- Nesbitt, S. W., E. J. Zipser, and D. J. Cecil (2000), A census of precipitation features in the tropics using TRMM: Radar, ice scattering, and lightning observations, *J. Clim.*, *13*, 4087–4106.
- Partain, P. (2007), CloudSat ECMWF-AUX auxiliary data process description and interface control document, *CIRA Tech. Rep. 5.2*, 10 pp., Colo. State Univ., Fort Collins.
- Polonsky, I. N., L. C. Labonnote, and S. Cooper (2008), Level 2 cloud optical depth product process description and interface control document, Version 5.0. CloudSat Project, CIRA, 21 pp., Colo. State Univ., Fort Collins.
- Posselt, D. J., S. C. van den Heever, and G. L. Stephens (2008), Trimodal cloudiness and tropical stable layers in simulations of radiative convective equilibrium, *Geophys. Res. Lett.*, *35*, L08802, doi:10.1029/2007GL033029.
- Probst, P., R. Rizzi, E. Tosi, V. Lucarini, and T. Maestri (2012), Total cloud cover from satellite observations and climate models, *Atmos. Res.*, *107*, 161–170, doi:10.1016/j.atmosres.2012.01.005.
- Ramanathan, V., and W. Collins (1991), Thermodynamic regulation of ocean warming by cirrus clouds deduced from observations of the 1987 El Niño, *Nature*, *351*, 27–32.
- Randall, D., M. Khairoutdinov, A. Arakawa, and W. Grabowski (2003), Breaking the cloud parameterization deadlock, *Bull. Am. Meteorol. Soc.*, *84*(11), 1547–1564, doi:10.1175/BAMS-84-11-1547.
- Riley, E. M., and B. E. Mapes (2009), Unexpected peak near  $-15^{\circ}\text{C}$  in CloudSat echo top climatology, *Geophys. Res. Lett.*, *36*, L09819, doi:10.1029/2009GL037558.
- Riley, E. M., B. E. Mapes, and S. N. Tulich (2011), Clouds associated with the Madden-Julian Oscillation: A new perspective from CloudSat, *J. Atmos. Sci.*, *68*, doi:10.1175/JAS-D-11-030.1.
- Sabin, T. P., C. A. Babu, and P. V. Joseph (2013), SST-convection relation over tropical oceans, *Int. J. Climatol.*, *33*(6), 1424–1435, doi:10.1002/joc.3522.
- Sassen, K., and Z. Wang (2008), Classifying clouds around the globe with the CloudSat radar: 1-year of results, *Geophys. Res. Lett.*, *35*, L04805, doi:10.1029/2007GL032591.
- Sassen, K., Z. Wang, and D. Liu (2009), Cirrus clouds and deep convection in the tropics: Insights from CALIPSO and CloudSat, *J. Geophys. Res.*, *114*, D00H06, doi:10.1029/2009JD011916.
- Sellers, S., P. Nguyen, W. Chu, X. Gao, K.-L. Hsu, and S. Sorooshian (2013), Computational Earth science: Big data transformed into insight, *Eos Trans. AGU*, *94*, 277–278, doi:10.1002/2013EO320001.
- Singh, M. S., and P. A. O’Gorman (2013), Upward shift of the atmospheric general circulation under global warming: Theory and simulations, *J. Clim.*, *25*, doi:10.1175/JCLI-D-11-00699.1.
- Stephens, G. L. (2005), Cloud feedbacks in the climate system: A critical review, *J. Clim.*, *18*, 237–273.
- Stephens, G. L., et al. (2002), The Cloudsat mission and the A-Train, *Bull. Am. Meteorol. Soc.*, *83*(12), 1771–1790, doi:10.1175/BAMS-83-12-1771.
- Stephens, G. L., et al. (2008), CloudSat mission: Performance and early science after the first year of operation, *J. Geophys. Res.*, *113*, D00A18, doi:10.1029/2008JD009982.
- Stevens, B. (2005), Atmospheric moist convection, *Ann. Rev. Earth Planet. Sci.*, *33*, 605–643, doi:10.1146/annurev.earth.33.092203.122658.
- Stubenrauch, C. J., A. Chédin, G. Rädcl, N. A. Scott, and S. Serrar (2006), Cloud properties and their seasonal and diurnal variability from TOVS Path-B, *J. Clim.*, *19*, 5531–5553.
- Wang, Z., and K. Sassen (2007), Level 2 cloud scenario classification product process description and interface control document, *CIRA Tech. Rep. 5.0*, 50 pp., Colo. State Univ., Fort Collins.
- Wood, N. (2008), Level 2 radar-visible optical depth cloud water content process description document, Version 5.1, CloudSat Project, CIRA, 26 pp., Colo. State Univ., Fort Collins.
- Wood, R. (2012), Stratocumulus clouds, *Mon. Weather Rev.*, *140*, 2373–2423, doi:10.1175/MWR-D-11-00121.1.
- Xu, K.-M., T. Wong, B. A. Wielicki, L. Parker, and Z. A. Eitzen (2005), Statistical analyses of satellite cloud object data from CERES. Part I: Methodology and preliminary results of the 1998 El Niño/2000 La Niña, *J. Clim.*, *18*, 2497–2514.
- Xu, K.-M., T. Wong, B. A. Wielicki, L. Parker, B. Lin, Z. A. Eitzen, and M. Branson (2007), Statistical analyses of satellite cloud object data from CERES. Part II: Tropical convective cloud objects during 1998 El Niño and evidence for supporting the fixed anvil temperature hypothesis, *J. Clim.*, *20*, 819–842.
- Young, A. H., J. J. Bates, and J. A. Curry (2013), Application of cloud vertical structure from CloudSat to investigate MODIS-derived cloud properties of cirriform, anvil, and deep convective clouds, *J. Geophys. Res. Atmos.*, *118*, 4689–4699, doi:10.1002/jgrd.50306.
- Yuan, J., and R. A. Houze (2010), Global variability of mesoscale convective system anvil structure from A-train satellite data, *J. Clim.*, *23*, 5864–5888.
- Yuter, S. E., R. A. Houze Jr., E. A. Smith, T. T. Wilheit, and E. Zipser (2005), Physical characterization of tropical oceanic convection observed in KWAJEX, *J. Appl. Meteorol.*, *44*, 385–415.
- Zelinka, M. D., and D. L. Hartmann (2010), Why is the longwave cloud feedback positive?, *J. Geophys. Res.*, *115*, D16117, doi:10.1029/2010JD013817.